Inorganic Chemistry
Cite This: Inorg. Chem. XXXX, XXX, XXX–XXX
Article
pubs.acs.org/IC

Law and Disorder: Special Stacking Units—Building the Intergrowth $Ce_6Co_5Ge_{16}$

Justin B. Felder,[†] Ashley Weiland,[†] Halyna Hodovanets,[§] Gregory T. McCandless,[†] Tania G. Estrada,[†] Thomas J. Martin,[†] Amy V. Walker,[†,‡] Johnpierre Paglione,[§,∥] and Julia Y. Chan*[,†]

[†]Department of Chemistry & Biochemistry and [‡]Department of Materials Science and Engineering, University of Texas at Dallas, Richardson, Texas 75080, United States

[§]Center for Nanophysics and Advanced Materials, Department of Physics, University of Maryland, College Park, Maryland 20742, United States

[∥]Canadian Institute for Advanced Research, Toronto, Ontario M5G 1Z8, Canada

Supporting Information

ABSTRACT: A new structure type of composition $Ce_6Co_5Ge_{16}$ was grown out of a molten Sn flux. $Ce_6Co_5Ge_{16}$ crystallizes in the orthorhombic space group *Cmcm*, with highly anisotropic lattice parameters of a = 4.3293(5) Å, b = 55.438(8) Å, and c = 4.3104(4) Å. The resulting single crystals were characterized by X-ray diffraction, and the magnetic and transport properties are presented. The Sn-stabilized structure of $Ce_6Co_5Ge_{16}$ is based on the stacking of disordered Ce cuboctahedra and is an intergrowth of existing structure types including AlB_2, $BaNiSn_3$, and $AuCu_3$. The stacking of structural subunits has previously been shown to be significant in the fields of superconductivity, quantum materials, and optical materials. Herein, we present the synthesis, characterization, and complex magnetic behavior of $Ce_6Co_5Ge_{16}$ at low temperature, including three distinct magnetic transitions.

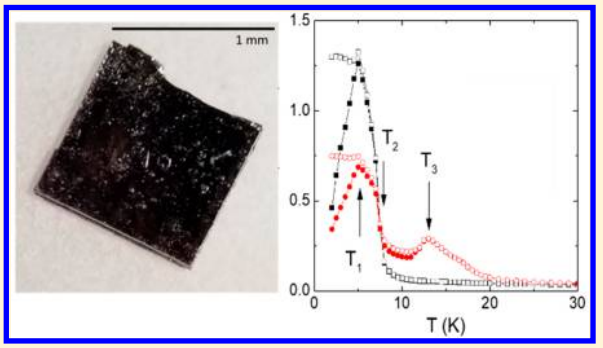

INTRODUCTION

To study the intrinsic physical and anisotropic properties of highly correlated quantum systems, the growth of single crystalline intermetallics is critical. With our ongoing efforts to grow single crystals of magnetic materials with competing magnetic interactions,[1] the opportunity exists to discover new compositions or robust structure types enabling subsequent substitution for correlation studies for compounds with competing magnetic behavior. Following the discovery of magnetically mediated superconductivity in Ce_nMIn_{3n+2} (n = 1, 2, ∞; M = Co, Rh, Ir), we are focusing our efforts on the crystal growth of structures with lanthanide-containing cuboctahedra in an intergrowth series.[2]

Cerium intermetallics containing group 14 elements exhibit a diverse range of physical properties.[3,4] $CePd_2Si_2$[5] and $CeCu_2Si_2$[6] for example exhibit magnetically mediated superconductivity. $CeNiGe_3$ and $Ce_2Ni_3Ge_5$ have been found to be pressure-induced unconventional superconductors.[7,8] $Ce_3Co_4Sn_{13}$ is reported to have a large Sommerfeld coefficient[9] indicating a heavy electron system ($\gamma \sim 4280$ mJ/mol K^2) with possible charge density waves.[10] A feature found in several of the Ce−Co−Ge intermetallics is the intergrowth of $AuCu_3$ and $CeNiSi_2$ with the noncentrosymmetric $BaNiSn_3$ subunit.[11] Several of the germanides, such as Ce_3CoGe_2, Ce_2CoGe_3, and $CeCoGe_3$, exhibit intermediate or valence fluctuation or superconductivity upon application of pressure.[12,13] More recently, we reported the crystal growth and magnetic properties of Sn-stabilized $Ln_3Co_2Ge_7$ (Ln = Pr, Nd, and Sm)[14] adopting the $La_3Co_2Sn_7$ structure type.[15] As part of our investigations of Ce-based germanides, we discovered a new structure type: $Ce_6Co_5Ge_{16}$. In this manuscript, we present the crystal growth, structure, and magnetic and transport properties of the Sn-stabilized structure $Ce_6Co_{5+x}Ge_{16-y}Sn_y$. For simplicity throughout the manuscript, the compound will be referred to as $Ce_6Co_5Ge_{16}$.

EXPERIMENTAL SECTION

Synthesis. $Ce_6Co_5Ge_{16}$ was found while pursuing the Ge analogue of the $La_3Co_2Sn_7$ structure type.[15] The compound can be prepared by combining Ce, Co, and Ge in a 6:5:16 stoichiometric ratio with 25 molar excess of Sn flux in an alumina crucible. This growth crucible was combined with a catch crucible separated by a frit, as described by Canfield.[16] The crucibles were then sealed in a fused-silica tube under ~$^1/_3$ atm of Ar gas. The sealed reaction vessel was placed inside a programmable furnace at 300 °C and heated to 1000 °C at a rate of 100°/h. Upon reaching 1000 °C, the furnace was allowed to dwell for 120 h before slowly cooling to 815 °C at a rate of 2°/h. After cooling to 815 °C, the reaction tube was quickly removed, inverted, and centrifuged to remove the excess molten Sn. Upon cooling, a high yield of >1 mm on edge, plate-like crystals were obtained, and residual

Received: February 5, 2019

DOI: 10.1021/acs.inorgchem.9b00350
Inorg. Chem. XXXX, XXX, XXX–XXX

flux was etched in dilute HCl and further sonicated. An example of a $Ce_6Co_5Ge_{16}$ crystal is shown in Figure 1.

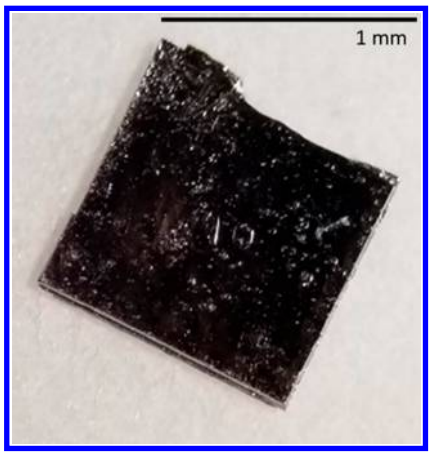

Figure 1. Photograph of a typical crystal of $Ce_6Co_5Ge_{16}$. Crystals are typically well-faceted square plates ranging in size from ~0.2 to ~10 mm on edge.

Structural Determination. Silver plate crystals were cut into appropriate sizes, and a crystal was mounted onto a glass fiber using epoxy. Single crystal X-ray diffraction data were collected on a Bruker D8 Quest Kappa single crystal X-ray diffractometer equipped with an IμS microfocus source (Mo Kα, λ = 0.71073 Å), a HELIOS optics monochromator, and a PHOTON II CPAD detector. The Bruker Saint program was used to integrate the diffraction profiles, while the scaling and absorption correction were performed using the Bruker program SADABS 2016/2 (multi−scan method).[17] Preliminary models of $Ce_6Co_{5+x}Ge_{16-y}Sn_y$ were generated using intrinsic phasing methods in SHELXT,[18] and anisotropically refined using SHELXL2014.[19] The full collection parameters and crystallographic data for $Ce_6Co_{5+y}Ge_{16-y}Sn_y$ are presented in Table 1. The atomic positions for $Ce_6Co_{5+y}Ge_{16-y}Sn_y$ are presented in Table 2. Figure 2 shows the crystal structure of $Ce_6Co_{5+y}Ge_{16-y}Sn_y$.

Table 1. Crystal Data, Data Collection, and Refinement Parameters

formula	$Ce_6Co_{5.472}Ge_{15.376}Sn_{0.624}$
space group	*Cmcm*
a (Å)	4.3293(5)
b (Å)	55.438(8)
c (Å)	4.3104(4)
V (Å^3)	1034.5(3)
Z	2
temperature (K)	298
θ (deg)	5.0−36.4
μ (mm^{-1})	39.79
reflections	71871
unique reflections	1532
data/restraints/parameters	1532/1/70
R_{int}	0.046
h	$-7 \le h \le 7$
k	$-92 \le k \le 92$
l	$-7 \le l \le 7$
$\Delta\rho_{max}$ (e Å^{-3})	5.75
$\Delta\rho_{min}$ (e Å^{-3})	−5.47
GoF	1.23
extinction coefficient	0.00013(3)
R_1 ($F^2 > 2\sigma(F^2)$)	0.037
wR_2 (F^2)	0.109

Table 2. Fractional Atomic Coordinates and Isotropic Displacement Parameters (Å^2)

	x	*y*	*z*	U_{eq}	occ. (<1)
Ce1	0	0.29456(2)	$^1/_4$	0.00984(13)	
Ce2	0	0.11659(2)	$^1/_4$	0.00703(12)	
Ce3	0	0.46949(2)	$^1/_4$	0.00726(12)	
Co1	0	0.35451(2)	$^1/_4$	0.0090(2)	
Co2	0	0.05661(2)	$^1/_4$	0.0056(2)	
Co1C	0	0.23373(4)	$^1/_4$	0.0148(5)	0.623(3)
Co2C	0	0.1775(2)	$^1/_4$	0.0148(5)	0.117(2)
Ge2	0	0.83768(2)	$^1/_4$	0.00897(19)	
Ge3	0	0.66232(2)	$^1/_4$	0.00944(19)	
Ge4	0	0.75002(2)	$^1/_4$	0.0116(2)	
Ge5	0	0.39565(2)	$^1/_4$	0.0080(2)	0.954(3)
Ge6	0	0.57375(2)	$^1/_4$	0.00742(18)	
Ge7	0	0.92620(2)	$^1/_4$	0.0066(3)	0.964(6)
Ge8	0	0.01381(2)	$^1/_4$	0.00689(17)	
Ge1B	0	0.19272(5)	$^1/_4$	0.0124(3)	0.623(3)
Ge2B	0	0.21879(18)	$^1/_4$	0.0080(2)	0.117(2)
Sn1A	0	0.20541(7)	$^1/_4$	0.0161(7)	0.260(3)
Sn2A	0	0.38464(4)	$^1/_4$	0.0161(7)	0.046(3)

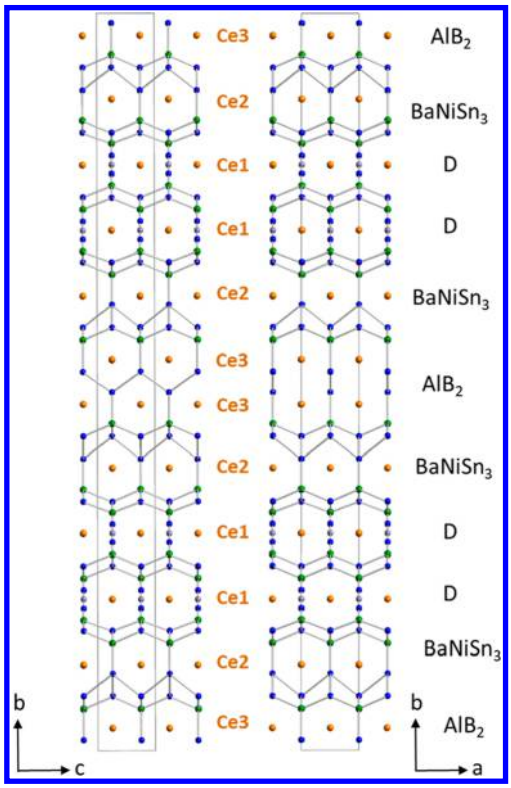

Figure 2. Crystal structure of $Ce_6Co_5Ge_{16}$ showing all of the Ce sites and the corresponding subunits which build the structure. Ce, Co, Ge, and Sn atoms are represented as orange, green, blue, and gray spheres, respectively. Left: view down the *a* axis. Right: view down the *c* axis. "D" denotes the disordered Ce1 site.

While evaluating the precession images, we observed periodic reflections in the [*h* 0 *l*] plane, with an approximate vector of [$^1/_2$ 0 $^1/_2$]. These reflections are very weak (<1% of the surrounding Bragg reflections), so they were not indexed. Attempts to solve the structure in lower symmetry space groups to account for these reflections were unsuccessful, and so our best average structural model is presented.

$Ce_6Co_{5+x}Ge_{16-y}Sn_y$ consists of three Ce sites, four Co sites, nine Ge sites, and one Sn site. Ce1 is in the center of an elongated

DOI: 10.1021/acs.inorgchem.9b00350
Inorg. Chem. XXXX, XXX, XXX−XXX

cuboctahedron which contains disordered Co (Co1C, Co2C), Ge (Ge1B, Ge2B), and Sn (Sn1A). These disordered sites are observed above and below the equatorial plane of the Ce1 cuboctahedral environment. The occupancy for each site (Sn1A, Ge1B, Ge2B, Co1C, Co2C) was initially allowed to refine freely, and the occupancies for Ge1B and Co1C were found to be similar, as were the occupancies for Ge2B and Co2C. The occupancies of these atom pairs were then constrained to be the same value, and the sum of the site occupancies was constrained to unity. This results in a polyhedral environment containing Sn1A only (case 1, 26%), Ge1B and Co1C (case 2, 62.3%), or Ge2B and Co2C (case 3, 11.7%). Figure S1 depicts how the disorder is modeled in the Ce1 polyhedron, similar to that of $Pr_3Co_{2+x}Ge_{7-y}Sn_y$.[14]

Additionally, the Ce2 site contains a disordered local environment, with Ge5 and Sn2A being partially occupied. Ge5 is present in ~95% of unit cells, while Sn2A is present in only ~5% of cells. Since Sn2A has such a low occupancy, it is omitted from our figures for clarity.

X-ray Photoelectron Spectroscopy. Ex situ X-ray photoelectron spectra (XPS) were obtained using a PHI Versa Probe II Scanning XPS Microprobe (Physical Electronic Inc., Chanhassen MN) equipped with an Al Kα X-ray source (E_p = 1486.7 eV). During measurement the chamber pressure typically was lower than 5×10^{-10} mbar. High-resolution spectra were collected with energy step 0.2 eV, analysis angle 45°, and pass energy 23.5 eV. Prior to data collection, the sample was sputtered for 15 min using an argon gas-cluster ion beam (Ar GCIB) to ensure any adventitious carbon, oxygen, or flux species were removed. All spectra were acquired using a charge compensation system equipped with both electron and ion beams incident on the surface. The binding energies were calibrated using the C 1s binding energy (284.8 eV).[20] The spectra were analyzed using CasaXPS 2.3.19PR1.0 (RBD Instruments, Inc., Bend, OR).

Physical Properties. After structural characterization, one large crystal was selected for physical property measurements. The crystal was oriented with respect to its crystallographic axes before measurements. Additionally, a small fragment was cleaved from the large crystal (after completion of the measurements) and characterized by single-crystal X-ray diffraction in order to confirm the structure of the measured crystal. Temperature- and field-dependent magnetization data were collected using either the Magnetic Properties Measuring System (MPMS) (1.8−300 K temperature range and 7 T magnetic field) or the Vibrating Sample Magnetometer (VSM) option of the Physical Properties Measurement System (PPMS) (1.8−300 K temperature range and 14 T magnetic field). GE varnish was used to secure the sample for the VSM measurements. The crystal was mounted in between two straws for the measurements in the MPMS. The PPMS was used to provide the temperature and field environment for electrical resistivity and heat capacity measurements. The electrical resistivity was measured using the standard four-probe method, where the gold wires for electrical current and voltage were attached to the sample using silver paste. Heat capacity measurements were performed using a standard relaxation technique.

RESULTS

Structure of $Ce_6Co_5Ge_{16}$. The unit cell is built by the stacking of several subunits constructed from the three Ce sites. The assignment of the subunits was guided by the work of Bobev et al.[21,22] These subunits consist of common intermetallic structure types and $Ce_6Co_5Ge_{16}$ can be thought of as an intergrowth of these structural subunits. As shown in Figure 2, $Ce_6Co_5Ge_{16}$ is built (from top to bottom) of the AlB_2, $BaNiSn_3$, D, D, $BaNiSn_3$, AlB_2, $BaNiSn_3$, D, D, $BaNiSn_3$, and AlB_2 structural type subunits. These intergrowth slabs are interspersed by a slab of Ce1 atoms with a highly disordered local environment, denoted as "D" as shown in Figure S1a. In case 1, where only Sn is present on the cuboctahedron's equator (Figure S1b), the Ce1 environment adopts the $AuCu_3$ subunit. In case 2 (Ge1B and Co1C; Figure S1c) and case 3 (Ge2B and Co 2C; Figure S 1d), the Ce 1 environment adopts the $BaNiSn_3$ type subunit. The bulk of the structure is built of slabs consisting of Ce3 atoms adopting the AlB_2 subunit intergrown into mirrored $BaNiSn_3$ type subunits of Ce2 atoms. The mirrored pairs of $BaNiSn_3$ subunits allows an inversion center to be present in $Ce_6Co_5Ge_{16}$.

The structure of $Ce_6Co_5Ge_{16}$ consists of stacked Ce environments along the b direction, giving rise to the long lattice parameter (~55 Å). There are three unique Ce sites along the b axis, and it makes sense to describe the structure in terms of the unique Ce sites. Ce1 resides in the center of a face-sharing cuboctahedron made up primarily of Co and Ge atoms. This cuboctahedron is characterized by disorder along the edges above and below the equatorial plane, as shown in Figure S1. The distance from Ce1 to the equatorial site (~3.0 Å) is more suitable for Sn than Ge or Co, so it is reasonable to model Sn at the equatorial positions with Ge (~3.1 Å) and Co (~3.4 Å) above and below. The mixing of the larger Sn atom serves to expand the lattice in order to accommodate the Ce in its polyhedral environment. The Ce1 polyhedra pack in an AB arrangement forming a staggered double-layer of Ce1 atoms. There are two distinct Ce1−Ce1 interactions. In Figure S2, the local Ce1 coordination environment is shown along with the extended Ce1 slab. The first two interactions are between Ce1 atoms within the same [ac] plane which are moderately long at 4.3104(4) and 4.3293(5) Å. The third contact, which is between the first and second "layers" of the double-layered slab, is quite long at 5.809(1) Å.

As shown in Figure S3, the Ce2 atoms are surrounded by 12 Ge atoms and 6 Co atoms. Each polyhedral unit face-shares with polyhedra in both the a and c directions forming a slab of Ce2 atoms. The Ce2−Ce2 contacts are similar to the Ce1−Ce1 contacts at ~4.3 Å. Interestingly, the interactions between the Ce1 atoms and Ce2 atoms is roughly the same as the long Ce1−Ce1 contact at ~5.80 Å. Although the Ce1 and Ce2 atoms reside in "closed units", the Ce3 atoms can be thought of residing in an "open" or "half-unit" like environment consisting of 9 Ge and 4 Co atoms. Figure 3 shows the local environment of Ce3 forming "$CeCoGe_2$" of the $CeNiSi_2$-type along the b direction, similar to what is observed in $U_3Co_2Ge_7$.[21] Although Ce3 also forms a double-layer like Ce1, the two different Ce3−Ce3 interactions are equal in

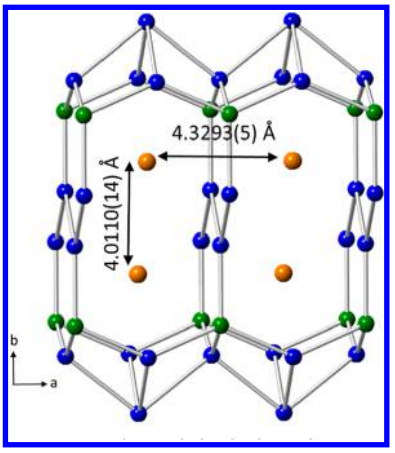

Figure 3. Polyhedral environment of Ce3, which is the AlB_2 structural subunit within $Ce_6Co_5Ge_{16}$. Ce3−Ce3 contacts in the b direction are close, with pairs of Ce3 atoms residing in a single polyhedron. Each polyhedral unit forms channels down the c direction and are face-shared in the a direction.

DOI: 10.1021/acs.inorgchem.9b00350
Inorg. Chem. XXXX, XXX, XXX−XXX

length at ~4.01 Å, giving rise to the potential for strong interactions between Ce3 atoms. Together these Ce3 half units form zigzag chains running in the *c* direction. These chains are connected in the *a* direction forming Ce3 double-layer slabs. A list of Ce−Ce distances are given in Table 3, ranging from 4.0110(14) to 5.6660(14) Å.

Table 3. Ce−Ce Interatomic distances (Å)

Ce1−Ce1 (×2)	4.3104(4)
Ce1−Ce1 (×2)	4.3293(5)
Ce2−Ce2 (×2)	4.3104(4)
Ce2−Ce2 (×2)	4.3293(5)
Ce3−Ce3 (×2)	4.0110(14)
Ce3−Ce3 (×2)	4.3104(4)
Ce3−Ce3 (×2)	4.3293(5)
Ce2−Ce3 (×4)	5.6660(14)

X-ray Photoelectron Spectroscopy of $Ce_6Co_5Ge_{16}$. Figure S4 displays high-resolution X-ray photoelectron spectra of a $Ce_6Co_5Ge_{16}$ single crystal. The Ce 3d photoelectron spectrum shows a doublet corresponding to the Ce $3d_{5/2}$ and $3d_{3/2}$ states separated by 18.3 eV. Furthermore, the Ce $3d_{5/2}$ state can be fitted to two peaks at 881.4 and 885.2 eV which are assigned to the v_0 and v' states of Ce^{3+}, respectively.[23,24] Similarly, the Ce $3d_{3/2}$ state can be fit to 899.9 and 903.5 eV which are assigned to the u_0 and u' states of Ce^{3+}, respectively. No evidence of Ce in the 4+ oxidation state is observed.[25,26] The Co 2p photoelectron spectrum indicates that the Co present is primarily as Co (0) ($2p_{3/2}$: 778.8 eV; $2p_{1/2}$: 792.8 eV).[27] The data also show that there is a small amount of Co present in a higher oxidation state, a mixed Co^{2+} and Co^{3+} state.[27−30] Finally, we note that there is a small amount of Sn present in the sample even after extensive sputtering using an Ar GCIB. This suggests that a small amount of Sn is incorporated in the crystal lattice. The data indicate that the Sn is present as Sn(0) ($3d_{5/2}$: 484.6 eV; $3d_{3/2}$ 493.0 eV) and Sn^{2+} ($3d_{5/2}$: 485.9 eV; $3d_{3/2}$ 494.6 eV).[31,32]

Magnetic Properties. The temperature-dependent magnetization data of a $Ce_6Co_5Ge_{16}$ single crystal is shown in Figure 4a. From the Curie−Weiss fit of the data for *H*||*a*, *H*||*b*, and *H*||*c*, and polycrystalline average *H*/*M* data above 150 K, the effective moment is estimated to be $\mu_B{}^a$ = 2.34 μ_B, $\mu_B{}^b$ = 2.54 μ_B, $\mu_B{}^c$ = 2.34 μB, and $\mu_B{}^{poly}$ = 2.53 μ_B, which is consistent with the effective moment of Ce^{3+} free ions, and the Weiss constant is estimated to be $\theta_p{}^a$ = −152.8 K, $\theta_p{}^b$ = −82.4 K, $\theta_p{}^c$ = −19.4 K, and $\theta_p{}^{poly}$ = −66.5 K, which indicates dominant antiferromagnetic interactions. Because the effective moment obtained is close to that of the Ce^{3+} free ion (2.54 μ_B), the magnetism of $Ce_6Co_5Ge_{16}$ is likely due to the 4f-electrons of Ce. The compound orders magnetically at 7.5, 12.0, and 16.0 K. The ordering temperatures were determined from a plot of $d(M(T)T/H)/dT$. The three magnetic transitions are clearly seen in the zero-field cooled (ZFC) and field-cooled (FC) susceptibility data for *H*||*b*, as shown in Figure 4a. Large magnetic anisotropy between the crystallographic *c*-axis and *a*- and *b*-axes indicates that the *c*-axis is an easy axis, as shown in Figure 4a,b.

The large magnetic anisotropy is also clearly seen in the $M(H)$ data at ~2 K. The $M(H)$ data for *H*||*a* and *H*||*b* have metamagnetic transitions below 2 T. The $M(H)$ data for *H*||*c* shows hysteresis. The steep rise of the magnetization for *H*||*c* results in the extreme sensitivity of the measurement to the remnant field and as can be seen in Figure 5a results in the nonzero moment at H = 0 without proper demagnetization. The hysteresis loops after demagnetization for *H*||*c* at 1.8 and 4.5 K, both in the ordered state below T_1, are shown in Figure 5b. The coercive field is about 0.0265 T at 1.85 K. The coercive field is almost 0 at 4.5 K.

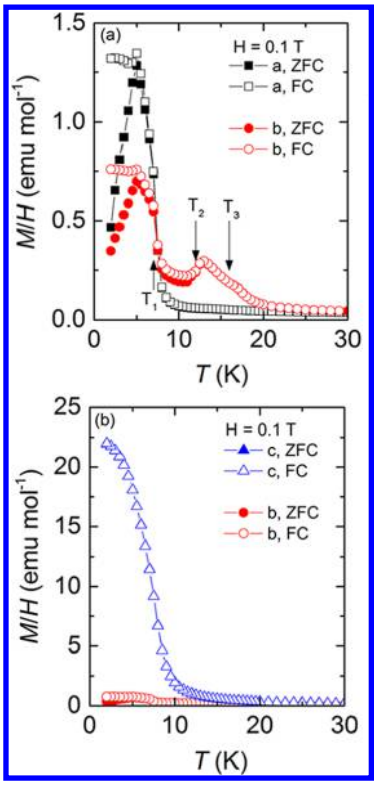

Figure 4. (a) ZFC and FC temperature-dependent magnetization data for *H*||*a* and *H*||*b*. The three magnetic ordering temperatures are marked with the arrows. (b) ZFC and FC magnetization for *H*||*b* and *H*||*c*. Here the $M(T)$ data for *H*||*b* are repeated for comparison.

Heat Capacity and Resistivity. Figure 6 shows the temperature dependent heat capacity measured at H = 0 T. The three magnetic ordering temperatures are clearly observed in the heat capacity measurements. As seen in the inset, the Sommerfeld coefficient of 80 mJ/(mol-Ce K^2), estimated from the linear fit if $C(T)/T$ versus T^2 above T_3 indicates an enhancement of the electron effective mass. Figure 7 shows the temperature-dependent resistivity of a $Ce_6Co_5Ge_{16}$ single crystal down to 1.8 K. The sample is metallic down to 150 K followed by a broad feature down to 2 K, which is likely due to the thermal depopulation of excited crystal-electric-field levels. The superconducting transition seen at 3.7 K is due to the elemental Sn that was used as flux for the crystal growth.

DISCUSSION AND CONCLUSION

Since the observed magnetic moment agrees quite well with the calculated moment for the Ce^{3+} free ion,[33] we can assume that all magnetic ordering arises from Ce atoms in the structure. As shown in Figure 4, the temperature-dependent magnetization measured with the field applied parallel to the *c*-axis is much greater than the with the field applied parallel to the *a*- or *b*-axes, indicating an easy axis of magnetization. All three crystallographic Ce sites have close contacts in the [*ac*] plane, with bond distances which are identical across all sites. Ce−Ce contacts along the *a*- and *c*-axis are 4.3293(6) and

DOI: 10.1021/acs.inorgchem.9b00350
Inorg. Chem. XXXX, XXX, XXX−XXX

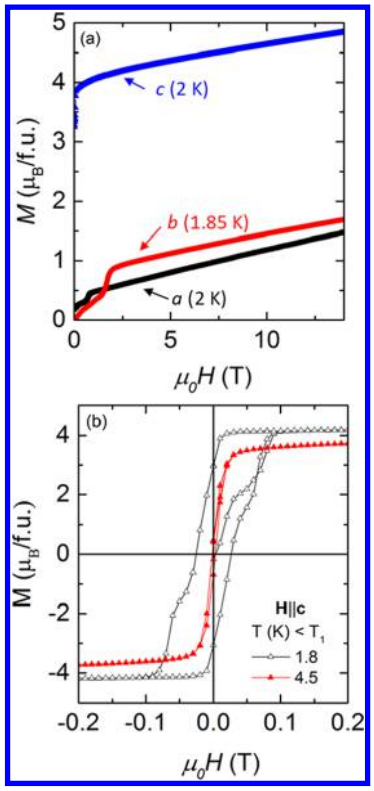

Figure 5. (a) $M(H)$ data for $H\|a$, $H\|b$, and $H\|c$. (b) Hysteresis loops for $H\|c$ collected at 1.8 and 4.5 K.

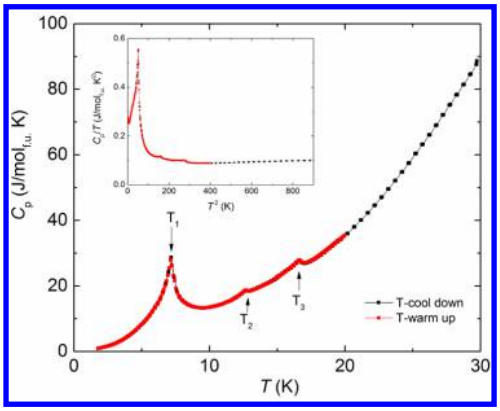

Figure 6. Heat capacity $C_p(T)$ of $Ce_6Co_5Ge_{16}$ single crystal. The three magnetic ordering temperatures are shown with the arrows. The inset shows $C_p(T)/T$ versus T^2 data.

4.3104(4) Å, respectively. T_3 manifests as a local maximum at 16.0 K in the susceptibility data, indicating antiferromagnetic interactions.

The transitions which occur at lower temperatures, T_1 (7.5 K) and T_2 (12.0 K), have contributing interactions in both the a and b directions. There is only one type of Ce−Ce interaction below the Hill limit[34,35] with interatomic contacts in both of the contributing directions: Ce3−Ce3 with a contact of 4.0110(14) Å. Since the magnetic coupling constant, J, is proportional to interatomic separation, it would make sense to associate this relatively short interaction with the higher temperature transition T_2. T_2 is accompanied by a sharp increase in susceptibility, indicating ferromagnetic-like ordering. Despite this, no field dependence is observed above 4.5 K. Since this is the only close Ce−Ce interaction along the

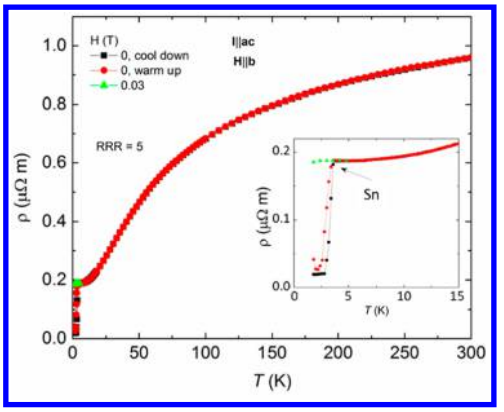

Figure 7. Temperature-dependent resistivity of $Ce_6Co_5Ge_{16}$. The superconducting transition is due to elemental Sn (H_c = 0.03 T) used as a flux to grow single crystals. The inset shows enlarged low-temperature part of $\rho(T)$.

appropriate directions, we must assume that T_1 also involves this interaction. T_1 occurs along with clear field dependence observable in both the susceptibility and $M(H)$ plots (Figure 5b). Given the stepwise increase in magnetization with $H\|c$, we attribute the transition to a spin reorientation.

We can also attribute the observed magnetic properties to the structural subunits that build the structure. One such subunit in $Ce_6Co_5Ge_{16}$ is $CeCoGe_3$ of the $BaNiSn_3$ type (Figure 2).[36] We hypothesize that the $CeCoGe_3$ sublattice is contributing magnetic behavior to $Ce_6Co_5Ge_{16}$. $CeCoGe_3$ exhibits three magnetic transitions: $T_1 \sim 7.75$ K, $T_2 \sim 11.75$ K, and $T_3 \sim 20.5$ K.[12,37] These transition temperatures are quite similar to the transition temperatures we observe in $Ce_6Co_5Ge_{16}$: T_1 = 7.5 K, T_2 = 12.0 K, T_3 = 16.0 K. The magnetic properties of $CeCoGe_3$ have been studied extensively by techniques such as SQUID magnetometry, μSR, and neutron diffraction.[37] At 14 K, after the highest temperature transition, the magnetic structure represents an antiferromagnet, with a slight ferromagnetic contribution from one Ce atom. As the temperature decreases, the structure becomes modulated through T_2 until settling into a 2-up, 2-down antiferromagnetic structure at 2 K.[37] Although the antiferromagnetic ground state presented for $CeCoGe_3$ does not agree with the more ferromagnetic-like $Ce_6Co_5Ge_{16}$, it is possible that a similar mechanism drives the magnetic ordering where T_2 observed in $Ce_6Co_5Ge_{16}$ represents an intermediate magnetic structure along the way to a canted antiferromagnetic ground state below T_1. Neutron diffraction studies would provide insights into the magnetic structure of $Ce_6Co_5Ge_{16}$. With a careful examination of the structure and bond distances of $Ce_6Co_5Ge_{16}$ coupled with the magnetic data, we can make physically reasonable assertions about the microscopic nature of the observed magnetic properties in this new structure type. We have presented a new structure type, $Ce_6Co_5Ge_{16}$, and the anisotropic magnetic and transport properties measured on oriented single-crystals. Additionally, we have shown the stacking of structural subunits can serve as a playground to study the interactions of f-electrons with conduction electrons.

■ ASSOCIATED CONTENT

Supporting Information

The Supporting Information is available free of charge on the ACS Publications website at DOI: 10.1021/acs.inorgchem.9b00350.

DOI: 10.1021/acs.inorgchem.9b00350
Inorg. Chem. XXXX, XXX, XXX−XXX

Additional images of Ce coordination environments and images of Ce1 disorder model (PDF)

Accession Codes

CCDC 1891432 contains the supplementary crystallographic data for this paper. These data can be obtained free of charge via www.ccdc.cam.ac.uk/data_request/cif, or by emailing data_request@ccdc.cam.ac.uk, or by contacting The Cambridge Crystallographic Data Centre, 12 Union Road, Cambridge CB2 1EZ, UK; fax: +44 1223 336033.

AUTHOR INFORMATION

Corresponding Author

*E-mail: Julia.Chan@utdallas.edu.

ORCID

Justin B. Felder: 0000-0002-2528-1967
Ashley Weiland: 0000-0001-7198-3559
Amy V. Walker: 0000-0003-2114-3644
Julia Y. Chan: 0000-0003-4434-2160

Notes

The authors declare no competing financial interest.

ACKNOWLEDGMENTS

J.Y.C. acknowledges National Science Foundation grant # DMR-1700030 for support of this project. Experimental investigations at the University of Maryland were supported by the Gordon and Betty Moore Foundation's EPiQS Initiative through Grant No. GBMF4419. A.V.W. gratefully acknowledges the support from the National Science Foundation (CHE 1708259 and DMR 1609081).

REFERENCES

(1) Schmitt, D. C.; Drake, B. L.; McCandless, G. T.; Chan, J. Y. Targeted Crystal Growth of Rare Earth Intermetallics with Synergistic Magnetic and Electrical Properties: Structural Complexity to Simplicity. *Acc. Chem. Res.* **2015**, *48*, 612−618.

(2) Phelan, W. A.; Menard, M. C.; Kangas, M. J.; McCandless, G. T.; Drake, B. L.; Chan, J. Y. Adventures in Crystal Growth: Synthesis and Characterization of Single Crystals of Complex Intermetallic Compounds. *Chem. Mater.* **2012**, *24*, 409−420.

(3) Sologub, O. L.; Salamakha, P. S. Rare Earth - Antimony Systems. *Handb. Phys. Chem. Rare Earths* **2003**, *33*, 35−146.

(4) Morosan, E.; Natelson, D.; Nevidomskyy, A. H.; Si, Q. Strongly Correlated Materials. *Adv. Mater.* **2012**, *24*, 4896−4923.

(5) Mathur, N.; Grosche, F.; Julian, S.; Walker, I.; Freye, D.; Haselwimmer, R.; Lonzarich, G. Magnetically Mediated Superconductivity in Heavy Fermion Compounds. *Nature* **1998**, *394*, 39.

(6) Stockert, O.; Arndt, J.; et al. Magnetically Driven Superconductivity in $CeCu_2Si_2$. *Nat. Phys.* **2011**, *7*, 119.

(7) Nakashima, M.; Kohara, H.; et al. A Change of Electronic State Tuned by Pressure: Pressure-Induced Superconductivity of the Antiferromagnet $Ce_2Ni_3Ge_5$. *J. Phys.: Condens. Matter* **2005**, *17*, 4539.

(8) Nakashima, M.; Tabata, K.; et al. High-Pressure Effect on the Electronic State in $CeNiGe_3$: Pressure-Induced Superconductivity. *J. Phys.: Condens. Matter* **2004**, *16*, L255.

(9) Christianson, A. D.; Gardner, J. S.; Kang, H. J.; Chung, J. H.; Bobev, S.; Sarrao, J. L.; Lawrence, J. M. Low Temperature Behavior of the Heavy Fermion $Ce_3Co_4Sn_{13}$. *J. Magn. Magn. Mater.* **2007**, *310*, 266−267.

(10) Thomas, E. L.; Lee, H.-O.; Bankston, A. N.; MaQuilon, S.; Klavins, P.; Moldovan, M.; Young, D. P.; Fisk, Z.; Chan, J. Y. Crystal Growth, Transport, and Magnetic Properties of $Ln_3Co_4Sn_{13}$ (Ln = La, Ce) with a Perovskite-like Structure. *J. Solid State Chem.* **2006**, *179*, 1642−1649.

(11) Soudé, A.; Pikul, A. P.; Wiśniewski, P.; Tougait, O.; Pasturel, M.; Kaczorowski, D.; Noël, H. Magnetic, Electric and Thermoelectric Properties of Ternary Intermetallics from the Ce-Co-Ge System. *Intermetallics* **2011**, *19*, 1201−1206.

(12) Kaneko, K.; Metoki, N.; Takeuchi, T.; Matsuda, T. D.; Haga, Y.; Thamizhavel, A.; Settai, R.; Ōnuki, Y. Multi-Step Magnetic Transition in Non-Centrosymmetric Compound $CeCoGe_3$. *J. Phys.: Conf. Ser.* **2009**, *150*, 042082.

(13) Settai, R.; Sugitani, I.; Okuda, Y.; Thamizhavel, A.; Nakashima, M.; Ōnuki, Y.; Harima, H. Pressure-Induced Superconductivity in $CeCoGe_3$ Without Inversion Symmetry. *J. Magn. Magn. Mater.* **2007**, *310*, 844−846.

(14) Khan, M. A.; McCandless, G. T.; Benavides, K. A.; Martin, T. J.; Palacios, A. M.; Samuel, A. W. B.; Young, D. P.; Chan, J. Y. Crystal Growth and Magnetic Properties of $Pr_3Co_{2+x}Ge_7$ and the Sn-Stabilized $Ln_3Co_{2+x}Ge_{7-y}Sn_y$ (Ln = Pr, Nd, Sm). *Cryst. Growth Des.* **2018**, *18*, 6028−6034.

(15) Dörrscheidt, W.; Schäfer, H. Darstellung Und Kristallstruktur von $BaPdSn_3$, $SrPdSn_3$ und $La_3Co_2Sn_7$. *J. Less-Common Met.* **1980**, *70*, P1−P10.

(16) Canfield, P. C.; Kong, T.; Kaluarachchi, U. S.; Jo, N. H. Use of Frit-Disc Crucibles for Routine and Exploratory Solution Growth of Single Crystalline Samples. *Philos. Mag.* **2016**, *96*, 84−92.

(17) Krause, L.; Herbst-Irmer, R.; Sheldrick, G. M.; Stalke, D. Comparison of Silver and Molybdenum Microfocus X-ray Sources for Single-Crystal Structure Determination. *J. Appl. Crystallogr.* **2015**, *48*, 3−10.

(18) Sheldrick, G. M. SHELXT - Integrated Space-Group and Crystal-Structure Determination. *Acta Crystallogr., Sect. A: Found. Adv.* **2015**, *71*, 3−8.

(19) Sheldrick, G. M. Crystal Structure Refinement with SHELXL. *Acta Crystallogr., Sect. A: Found. Adv.* **2015**, *71*, 3−8.

(20) Barr, T. L.; Seal, S. Nature of the Use of Adventitious Carbon as a Binding Energy Standard. *J. Vac. Sci. Technol., A* **1995**, *13*, 1239−1246.

(21) Bobev, S.; Bauer, E. D.; Ronning, F.; Thompson, J. D.; Sarrao, J. L. Synthesis, Structure and Physical Properties of the New Uranium Ternary Phase $U_3Co_2Ge_7$. *J. Solid State Chem.* **2007**, *180*, 2830−2837.

(22) Suen, N.-T.; Huang, L.; Meyers, J. J.; Bobev, S. An Unusual Triple-Decker Variant of the Tetragonal BaAl4-Structure Type: Synthesis, Structural Characterization, and Chemical Bonding of $Sr_3Cd_8Ge_4$ and $Eu_3Cd_8Ge_4$. *Inorg. Chem.* **2018**, *57*, 833−842.

(23) Bêche, E.; Charvin, P.; Perarnau, D.; Abanades, S.; Flamant, G. Ce 3d XPS Investigation of Cerium Oxides and Mixed Cerium Oxide ($Ce_xTi_yO_z$). *Surf. Interface Anal.* **2008**, *40*, 264−267.

(24) Xiaosheng, H.; Guodong, Z.; Fang, D.; Zhicheng, T. An Environmentally Friendly Wide Temperature $CeWTiO_x$ Catalyst with Superior Performance for the Selective Catalytic Reduction NO_x with NH_3. *J. Ind. Eng. Chem.* **2019**, *69*, 66−76.

(25) Paparazzo, E. Use and Mis-Use of X-Ray Photoemission Spectroscopy Ce3d Spectra of Ce_2O_3 and CeO_2. *J. Phys.: Condens. Matter* **2018**, *30*, 343003.

(26) Kurleto, R.; Starowicz, P.; Goraus, J.; Baran, S.; Tyvanchuk, Y.; Kalychak, Y. M.; Szytuła, A. Electronic Structure and Transport Properties of $CeNi_9In_2$. *Solid State Commun.* **2015**, *206*, 46−50.

(27) Naumkin, A. V.; Kraut-Vass, A.; Gaarenstroom, S. W.; Powell, C. J. *NIST X-ray Photoelectron Spectroscopy Database*, version 4.1; National Institute of Standards and Technology: Washington, DC, 2012.

(28) Chuang, T. J.; Brundle, C. R.; Rice, D. W. Interpretation of the X-ray Photoemission Spectra of Cobalt Oxides and Cobalt Oxide Surfaces. *Surf. Sci.* **1976**, *59*, 413−429.

(29) Sexton, B. A.; Hughes, A. E.; Turney, T. W. An XPS and TPR Study of the Reduction of Promoted Cobalt-Kieselguhr Fischer−Tropsch Catalysts. *J. Catal.* **1986**, *97*, 390−406.

(30) Khassin, A. A.; Yurieva, T. M.; Kaichev, V. V.; Bukhtiyarov, V. I.; Budneva, A. A.; Paukshtis, E. A.; Parmon, V. N. Metal-Support Interactions in Cobalt-Aluminum Co-Precipitated Catalysts: XPS and CO Adsorption Studies. *J. Mol. Catal. A: Chem.* **2001**, *175*, 189−204.

DOI: 10.1021/acs.inorgchem.9b00350
Inorg. Chem. XXXX, XXX, XXX−XXX

(31) Li, J.-T.; Swiatowska, J.; Seyeux, A.; Huang, L.; Maurice, V.; Sun, S.-G.; Marcus, P. XPS and ToF-SIMS Study of Sn-Co Alloy Thin Films as Anode for Lithium Ion Battery. *J. Power Sources* **2010**, *195*, 8251−8257.
(32) Jie, L.; Chao, X. XPS Examination of Tin Oxide on Float Glass Surface. *J. Non-Cryst. Solids* **1990**, *119*, 37−40.
(33) Ashcroft, N. W.; Mermin, N. D. *Solid State Physics*; W.B. Saunders: Philadelphia, PA, 1976.
(34) Meisner, G. P.; Giorgi, A. L.; Lawson, A. C.; Stewart, G. R.; Willis, J. O.; Wire, M. S.; Smith, J. L. U_2PtC_2 and Systematics of Heavy Fermions. *Phys. Rev. Lett.* **1984**, *53*, 1829−1832.
(35) Rauchschwalbe, U.; Gottwick, U.; Ahlheim, U.; Mayer, H. M.; Steglich, F. Investigation of New Lanthanum-, Cerium- and Uranium-Based Ternary Intermetallics. *J. Less-Common Met.* **1985**, *111*, 265−275.
(36) Thamizhavel, A.; Takeuchi, T.; D Matsuda, T.; Haga, Y.; Sugiyama, K.; Settai, R.; Ōnuki, Y. Unique Magnetic Phases in an Antiferromagnet $CeCoGe_3$. *J. Phys. Soc. Jpn.* **2005**, *74*, 1858−1864.
(37) Smidman, M.; Adroja, D. T.; et al. Neutron Scattering and Muon Spin Relaxation Measurements of the Noncentrosymmetric Antiferromagnet $CeCoGe_3$. *Phys. Rev. B: Condens. Matter Mater. Phys.* **2013**, *88*, 134416.

DOI: 10.1021/acs.inorgchem.9b00350
Inorg. Chem. XXXX, XXX, XXX−XXX